

MPR Error Budget Analysis for Air or Space-borne Missile Surveillance

January 1999

Chiu-Kuang Chuang, M. Ronald Wohlers, James Stark Draper,
KTAADN, Inc., 1320 Centre St. Suite 201, Newton MA 02459
Howard Evans, Robert Cody,
Ball Aerospace and Technologies Corp., Huntsville, AL
Darren Sene,
NAIC, Huntsville, AL

The Monocular Passive Ranging (MPR) technique, applied from space or a high altitude airborne platform, provides a passive and covert means to establish 3-D position coordinates for tracking theater missiles during boost phase. This capability offers an application potential for missile surveillance and interceptor guidance [Draper et al., 1994, Perlman et al., 1996]. Earlier investigations also have shown that ranges derived from this methodology involved uncertainty associated with: (1) internal weather model, (2) internal missile signature modeling, (3) sensor look geometry accuracy, and (4) measurement data. In this work, analytical error budget assessments are carried out to account all error sources and rank their contributions. In brief, the background residual in measurement data is the most influential error source, dominating mainly on low altitude tracking whereas error induced by source uncertainty is ranked next and dominant at higher altitude tracking. The atmospheric modeling error is ranked third where the scale height uncertainty is more dominant than that of the extinction coefficient. And lastly, the sensor look geometry error is negligible if the pointing uncertainty is small, $<0.01\%$. The overall nominal total random range error is on the order of 2~5 % of the slant depth (path length through the atmosphere) and the magnitude increases drastically near both ends, near the ground and above 25-km altitudes.

1.0 Introduction

The Monocular Passive Ranging (MPR) technique is applied with IR sensors to track bright missile plumes at a distance and generate range coordinates¹. IR imaging sensors provide highly accurate angle-angle tracking. Augmenting them with range will enable the system to report missile 3-D position coordinates. Applying trajectory estimation on these 3-D coordinate sequence during boost phase tracking, the resultant track estimate offers various theater missile defense utilities, such as covert theater missile surveillance and missile impact prediction^{2,3}. Earlier investigations have also advanced the concept of integrating the MPR technique with UAV-based IR sensors to guide an on-board Kinetic Kill Vehicle (KKV) while it is loitering covertly inside enemy territory⁴. While many useful applications have already been addressed

¹ Jeffrey, W., Draper, J.S., Gobel, R., "Monocular Passive Ranging," 1994 IRIS Meeting of Specialty Group on Targets, Backgrounds and Discrimination, Volume II, pp 113 - 130, 213400-198-X(II) 1994.

² C.f. Jeffrey et al., IRIS 1994.

³ Perlman, S.E., Chuang, C.K., Draper, J.S., Powers, E.M., Frankel, D.S., Evans, H.E., Lillard, L.N., Jeffrey, W.A., Hibbeln, B.A., "Passive Ranging for Detection, Identification, Tracking and Launch Location of Boost Phase TBMs," IRIS Conference on Passive Sensors, March 1996, Monterey, CA.

⁴ Draper, J.S., Frederick, W., Smith, Col. W., "Assessment of MPR for UAV/KKV BPI," AIAA/BMDO Technology Conf., San Diego, CA, 18-22 Aug 1997.

Form SF298 Citation Data

Report Date <i>("DD MON YYYY")</i> 00011999	Report Type N/A	Dates Covered (from... to) <i>("DD MON YYYY")</i>
Title and Subtitle MPR Error Budget Analysis for Air or Space-borne Missile Surveillance		Contract or Grant Number
		Program Element Number
Authors		Project Number
		Task Number
		Work Unit Number
Performing Organization Name(s) and Address(es) KTAADN, Inc. 1320 Centre St. Suite 201 Newton MA 02459		Performing Organization Number(s)
Sponsoring/Monitoring Agency Name(s) and Address(es)		Monitoring Agency Acronym
		Monitoring Agency Report Number(s)
Distribution/Availability Statement Approved for public release, distribution unlimited		
Supplementary Notes		
Abstract		
Subject Terms		
Document Classification unclassified		Classification of SF298 unclassified
Classification of Abstract unclassified		Limitation of Abstract unlimited
Number of Pages 21		

and discussed, the ultimate utility of this methodology does depend on whether its inherent accuracy can satisfy an application's requirements or not. In this investigation, the range uncertainty of this methodology is analyzed using a detailed simulation approach augmented with first order analytic models that are of great utility in preliminary system studies and trade analysis. The goal is to estimate the total range error, including bias and random error sources, for various application assessments.

There are four key contributions to MPR⁵ range uncertainty: (1) internal weather modeling, both the atmospheric absorption coefficient and air density scale height, (2) internal missile signature modeling, both a changing mean and short-term fluctuations, (3) internal sensor look-geometry parameters, including the platform height and missile zenith angle, and (4) measurement data uncertainty, consisting of internal and external sensor noise associated with focal plane dark current, foreground and background radiation non-uniformity, etc.

In this report we establish an analytical foundation to account for the most important error sources pertaining to an MPR system. The goal is to identify the prominent error component in space-borne MPR operation and adopt a means for reducing total system error. Our efforts also included the estimation of the data and model parameter uncertainties pertaining to the MPR system. These make up the crucial foundation that determined the extent of MPR's total error budget.

2.0 MPR Range Equation and Error Budget

An MPR sensor deployed on a high earth orbit platform^{6,7} has a Line-of-Sight (LOS) whose full range (R_I) is the distance from the sensor to the target, but only a fraction of which, ($R_I - R_t$) called as the slant depth, passes through earth's atmosphere. Here R_t is the top of atmosphere, as indicated in Figure 1 where this relationship is graphically rendered.

⁵ Chuang, C.K., Draper, J.S., Perlman, S.E., Powers, E.M., Frankel, D.S., Evans, H.E., "An Autonomous Approach Toward Monocular Passive Ranging", 1997 Meeting of the IRIS Specialty Group on Targets, Backgrounds & Discrimination, Monterey CA, Feb, 1997 (U).

⁶ C.f. Perlman et al., IRIS 1996

⁷ C.f. Chuang et al, IRIS 1997.

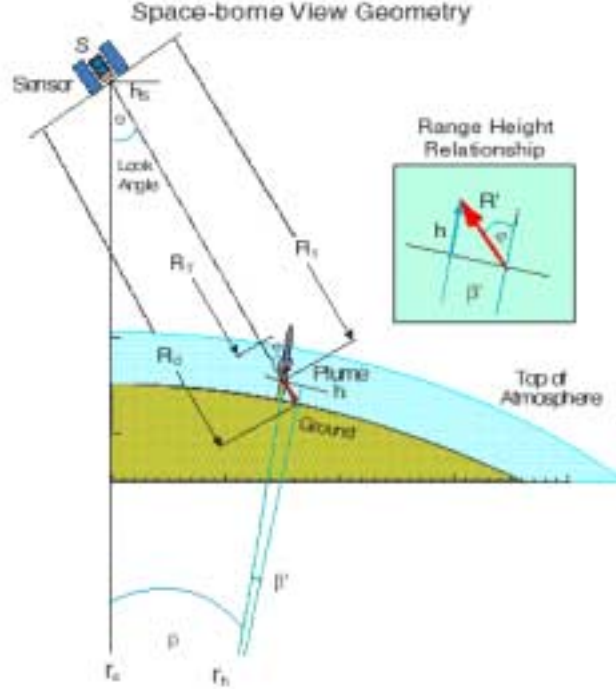


Figure 1. Sensor look geometry and two transmission components

The error budget analysis foundation for an MPR system is the range equation that is solved from equating the path transmittance to measured data, as to be described below.

2.1. MPR Signal Model

In atmospheric radiation transfer, the path transmission given by Beer's Law must be integrated over earth atmosphere with a changing air density. In addition, the air column is also self-emitting at ambient temperature, so-called foreground radiation^{8,9,10}. Thus, the target signal received at the sensor over band $\lambda_1 \sim \lambda_2$ is an apparent radiance of two component sum, $A_i(R)$ in $W/cm^2\text{-sr}$:

$$A_i = \frac{S_i}{\Delta \omega R^2} \tau_i + L_{ib}(1 - \tau_i), \quad \text{for } i = 1 \& 2 \quad (1)$$

Here the first term denotes the source signature decaying along the path with a transmittance $\tau_i(R_i - R_t)$ weighing an $1/R^2$ term (total range R_i), whereas the second term, $L_{bi}(R)$, denotes the self-emission and scattering from the foreground air column. S_i is given as total radiation power ($\pi a_p L_p$) with an area a_p and a unit area radiance of L_s in $W/cm^2\text{-sr}$. The transmission through this inhomogeneous medium is given by Beer's Law:

$$\tau = e^{-\alpha_0 \int_{R_t}^{R_i} e^{-h/H} dR} \quad (2)$$

where R_i and R_t denote the range, respectively, from the sensor to the target and to the top of the atmosphere along the LOS. Using the normal plane drawn at the ground intercepting point and

⁸ "Thermal Radiative Transfer and properties," Chapter 7 radiation transfer equation, Brewster M.Q., John Wiley & Sons, Inc., New York.,

⁹ cf Jeffrey et al., 1994.

¹⁰ Chiu-Kuang, Chuang, "Modeling Unresolved Target Detection Problems," IRIS 90 Specialty Group on Target, Background, and Detection, Albuquerque, NM, March 1990.

assuming an invariant target zenith angle, the Beer's Law integral can be integrated into a closed form transmittance, namely,

$$\tau = e^{-\frac{\alpha_o H}{\cos \varphi} \left[e^{-\frac{R' \cos \varphi}{H}} - e^{-\frac{R_T \cos \varphi}{H}} \right]} \quad (3)$$

where $R' = R_0 - R_1$, Plume to Ground Range
 $R_T = R_0 - R_T$, ATM top to Ground Range
 φ zenith angle

where R' is defined as the range from the target to the ground intercept point. Observing TBM from a space-borne platform at Highly Elliptical Orbit (HEO) or Geostationary Orbit (GO), the local zenith angle from the top of the atmosphere to the ground intercept point varies less than a fraction of a degree, except at near earth limb views. Thus, the closed form solution obtained here offers a good approximation. In addition, the second term will also diminished for $R_T \cos \varphi \gg H$ on $R_T \cos \varphi = 100$ km and $H = 6.7$ km scale height.

MPR as developed in Jeffrey et al's study is a dual band operation. The transmittance is formed by a two-band ratio, that is:

$$\tau_i \equiv \frac{\tau_2}{\tau_1} = e^{-\frac{(\alpha_{o2} - \alpha_{o1}) H}{\cos \varphi} e^{-\frac{R' \cos \varphi}{H}}} \quad (4)$$

assuming an identical scale height between two bands. The range can then be solved by equating Eq. 4 with measured data, B/C, which is defined below:

$$\tau_i = B/C \quad \text{where } B = \frac{(A_2 - L_{b2})}{(A_1 - L_{b1})}, \quad C = \frac{(\beta L_2 - L_{b2})}{(\beta L_1 - L_{b1})} \quad \text{and} \quad \beta = \frac{a}{\Delta \alpha R^2} \quad (5)$$

Here B and C denote, respectively, the measurement and source-radiance ratio between the band pair. β is the fraction of an IFOV that the target has subtended. In an unresolved target state ($0 < \beta < 1.0$) in which the missile plume is substantially brighter than foreground radiation ($L_{S2} \gg L_{b2}$), then $C = L_{S2}/L_{S1}$ and $B = A_2/A_1$. Thus, the range R' can be found as:

$$R' = -\frac{H}{\cos \varphi} \ln \left[\frac{\cos \varphi}{(\alpha_{o2} - \alpha_{o1}) H} \ln \frac{C}{B} \right] \quad (6)$$

where $R = R_0 - R'$ and $h = R' \cos \varphi$

This equation consists of parameters associating with source (C), atmospheric model (α_o and H), look geometry (φ), and measurement (B). Note this range equation forms the foundation for deriving the analytical error budget for all MPR's system components.

2.2 Total Random Range Error Budget

Let $f(.,.)$ represent Eq. 6, a continuous range equation, and using B , C , G , and M to indicate the generic system parameters. The range discrepancy for various MPR system sources can then be derived from Taylor expansion on the range function with respect to each system variable:

$$\Delta R = \frac{\partial f(.,.)}{\partial B} \Delta B + \frac{\partial f(.,.)}{\partial C} \Delta C + \frac{\partial f(.,.)}{\partial G} \Delta G + \frac{\partial f(.,.)}{\partial M} \Delta M \quad (7)$$

$$\text{and } \sigma^2 = E(\Delta R^2)$$

(8)

Based on $\sigma_X^2 = E(\Delta R_X^2)$ and assuming no mutual correlation among variables, all correlation terms, such as $E(\Delta B \Delta C)$, $E(\Delta B \Delta G)$, etc., are diminished:

$$\sigma_{R'}^2 = \sigma_B^2 + \sigma_C^2 + \sigma_G^2 + \sigma_M^2 \quad (9)$$

Here ΔB , ΔC , ΔG , and ΔM are the deviations from the mean of the measurement, source, geometry, and atmosphere, B_0 , C_0 , G_0 , M_0 , respectively. Thus, the four generic error components would be as following:

(1) σ_B , the measurement uncertainty

Since B is a ratio of two contrast signatures, A_2/A_1 , in which A_i can be treated as a mean \bar{A} superimposing with random fluctuation, viz., $A = \bar{A} + \varepsilon$. The sensitivity respect to this ΔB is given as:

$$\frac{df(.,.)}{dB} = \frac{H}{B \cos \varphi \ln(\frac{C}{B})} \quad (10)$$

$$\Delta B = B \left(\frac{\Delta A_2}{A_2} - \frac{\Delta A_1}{A_1} \right) \quad (11)$$

Here the data variance associated with measurement B must be accounted for both the variance and co-variance, viz.,

$$\sigma_B^2 = \sigma_{A1}^2 - 2\sigma_{A1}\sigma_{A2}\gamma_{21} + \sigma_{A2}^2$$

$$\text{Where Variance } \sigma_{Ai}^2 = E \left[\left(B \frac{\Delta A_i}{A_i} \right)^2 \right], \quad i = 1 \text{ or } 2 \quad (11-1)$$

$$\text{and Correlation Coefficient } \gamma_{21} = E \left[B \frac{\Delta A_2}{A_2} B \frac{\Delta A_1}{A_1} \right] / \sigma_{A1}\sigma_{A2}$$

In addition to this inter-band correlation, the noise in the in-band radiance A_1 and A_2 must also be taken into account their additive and multiplicative components, such as the following four terms model:

$$A_i = \bar{A}_i + \xi_{iD} + \xi_{iF} + \xi_{iK} + \xi_{iBS}, \quad i = 1 \text{ or } 2 \quad (11-2)$$

Since their origins are quite different, we resort to the general assumption of independence, thus the variance is a sum of the dark current, foreground radiation, pixel gain error, and background residual:

$$\sigma_B^2 = \sigma_D^2 + \sigma_F^2 + \sigma_K^2 + \sigma_{iBS}^2 \quad (11-3)$$

(2) σ_C , source-signature uncertainty

The sensitivity function of the source signature ratio, $C=L_2/L_1$, is:

$$\frac{df(.,.)}{dC} = -\frac{H}{C \cos \varphi \ln(\frac{C}{B})} \quad (12)$$

The signature uncertainty due to the temporal fluctuation of plume (random error term of the source signature) can be treated with identical procedure as B . For source signature data the inter-band correlation term, as given in Eq. 11-1, should also be taken into account, except on a toggling scheme where correlation would be far smaller.

(3) σ_G , geometry related uncertainty

As given in Eq. 6, the range equation is governed only by one geometrical term, i.e., the zenith angle of target. Thus, the sensitivity coefficient for this parameter is:

$$\frac{df(.,.)}{d\varphi} = \tan\varphi \left[f(.,.) + \frac{H}{\cos\varphi} \right] \quad (13)$$

(4) σ_M , atmospheric model uncertainty

This parameter consists of two terms, the extinction coefficient difference $D\alpha_0$ and the scale height H . Thus the sensitivity coefficient yields two terms:

$$\frac{df(.,.)}{dH} = -\frac{1}{\cos\varphi} \ln \left[\frac{\cos\varphi}{D\alpha_0 H} \ln\left(\frac{C}{B}\right) - 1 \right] \quad (14-1)$$

$$\frac{df(.,.)}{d\Delta\alpha_0} = \frac{H}{\cos\varphi D\alpha_0}, \quad \text{where } D\alpha_0 = (\alpha_{02} - \alpha_{01}) \quad (14-2)$$

3.0 Data Statistics and Simulation Analysis System

This section focuses on establishing all data statistics (1 σ deviation) that are required for determining the magnitude and functional dependency of the four classes of error source. Since these statistics are sensor system dependent, cautions must be paid in adopting data; compensation for difference in filter specs, detector type, telescope optics, as well as the target type and background are needed. We use one available missile signature campaign to establish a model of data statistics. The sensor used in this data campaign is an InSb FPA technology that is equipped with a large aperture. Its NEI is rated at 6.3×10^{-16} W/cm² and spatial resolution is in the order of 10 μ Rad.

3.1 MPR Filter Specification

The filter location and bandwidth for the space-borne sensor is given in Figure 2. These filters are specified as an idealized filter shape. F6 is located on the near transparent edge of the CO₂ absorption window which is used as a common reference for the four other test bands, F4, F3, F2, & F1. Using these bands and an estimation procedure on the two climate characterization coefficients, the transmission properties for these MPR bands can be quantitatively described.

3.2 Source Signature Data Statistics

The data set used here to characterize the plume and background data statistics was provided by SMDC/NRC at the Kennedy Space Center¹¹. It is a HERA missile launch collected at WSMR, NM in September 1997 using ISTEf sensor. The missile plume is observed at close range, 35 km away, for the first 30 (15 to 45s) seconds of the boost phase. The sensor is an IR tracker with a 24-inch aperture with 10- μ Rad IFOV and the target scene image is taken at 30-Hz frame rate. The target occasionally drifts out of view, partially or completely. The plume signature was frame-by-frame isolated and the average radiance was computed by summing all pixels. The count is then converted to radiance based on the calibration function provided by the ISTEf group.

¹¹ This data set was provided to us as a courtesy by SMDC/ISTEF through Alan Tiejian of Kennedy Space Center.

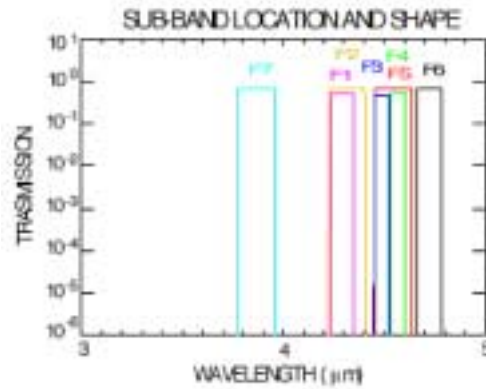


Figure 2. MPR operational filter banks defined in notional FPA.

- WSMR Missile Test
- 24 Inch Aperture
- SMDC/ISTEF w MPR Filter (F1 @4.72 μm)
- IFOV 10 μRad

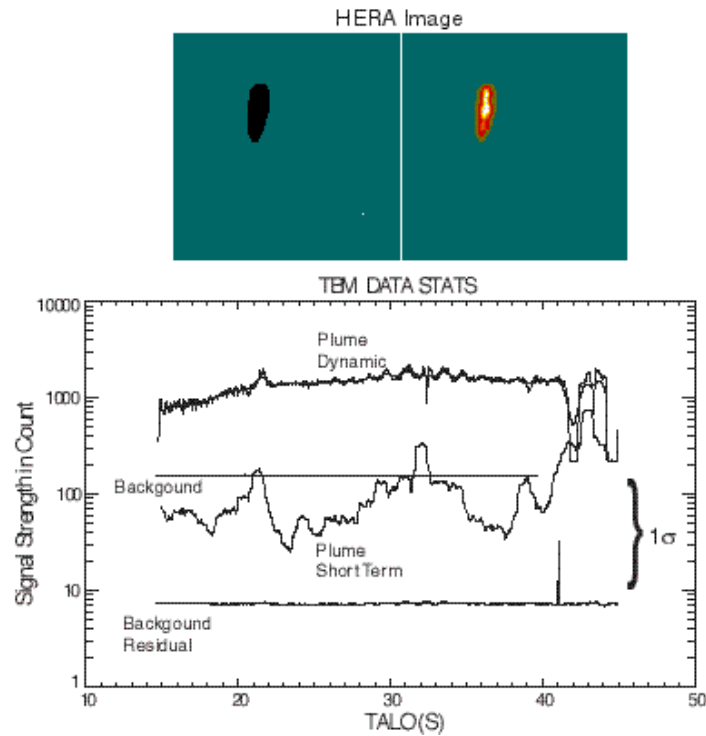


Figure 3. Source signature mean and short term temporal fluctuation.

The short-term temporal fluctuation was calculated as the difference from the moving average, a 1.5-second average window with a cosine weighting function known as a Hamming Window. The measured plume signature and its moving average are shown at the bottom plot of Figure 3 and tabulated in Table 1. The third column is the percentage fluctuation measured with respect to the mean.

A more representative short-term fluctuation was obtained by excluding large abrupt fluctuations. The result was a 2.0 to 4.5 % fluctuation with an average of 3.5%. This data fluctuation may be large, however, when the inter-band correlation is considered; the actual source-signature ratio uncertainty could be much smaller.

The spectral changes of the plume signature as a function of altitude is also important to the MPR range error because the plume radiation exhibits a systematic CO₂ emission peak shift from 4.6 μm to 4.4 μm with altitude. This is frequently observed in TBM. Figure 4 is a pseudo 3-D spectral intensity plot as a function of the missile altitude from 0 to 25-km and covering wavelengths from 2 μm to 5 μm . Because of this spectral peak shift phenomenon, the source signature ratio between two bands will not remain constant and will have to be modeled as a dynamic plume with a slow time function. The existing Autonomous MPR system has been upgraded to such a dynamic signature representation.

Table 1. Measured data statistics, mean and percentage short term Fluctuation for HERA and background residual fluctuation.

	TALO SM ^{*1}	TF ^{*1}	%	BM ^{*3}	BR ^{*4}	%
16	774.936	55.361	7.1	153.879	7.071	4.595
17	883.744	67.359	7.6	153.920	7.105	4.616
18	883.679	50.019	5.7	153.606	7.131	4.642
19	1008.484	58.696	5.8	154.204	6.948	4.505
20	1074.333	71.141	6.6	154.096	7.059	4.581
21	1092.216	88.456	8.1	154.069	7.070	4.589
22	1732.664	144.307	8.3	153.300	7.158	4.669
23	1435.911	41.994	2.9	153.907	6.947	4.514
24	1407.079	35.637	2.5	153.867	6.956	4.520
25	1332.630	43.760	3.3	153.736	6.828	4.441
26	1422.485	46.095	3.2	153.424	6.930	4.517
27	1548.740	50.479	3.3	153.488	6.901	4.496
28	1456.542	50.304	3.5	154.022	6.980	4.532
29	1768.531	78.959	4.5	153.583	7.158	4.660
30	1897.601	131.405	6.9	153.143	7.191	4.696
31	1568.324	149.506	9.5	153.180	7.089	4.628
32	1684.806	187.151	11.1	153.388	7.047	4.595
33	1923.165	133.517	6.9	153.244	7.212	4.706
34	1984.360	133.294	6.7	151.151	7.339	4.855
35	1843.613	117.413	6.4	152.464	7.183	4.712
36	1542.797	51.218	3.3	151.950	7.034	4.629
37	1494.835	46.486	3.1	151.955	7.019	4.619
38	1458.267	35.139	2.4	151.297	7.040	4.653
39	1488.409	124.902	8.4	151.734	6.956	4.585
40	1696.195	81.451	4.8	151.735	7.009	4.619
41	1553.578	119.021	7.7	152.664	6.876	4.504
42	499.813	342.610	68.5	171.702	7.096	4.133

^{*1} SM denotes source signature mean, ^{*2} TF denotes temporal fluctuation, ^{*3} BM background mean, and ^{*4} BR background residual.

3.3 Inter-Band Source Emission Correlation

Missile plume signature changes as a function of velocity and altitude. A modeled SCUD missile source signatures¹² at twelve altitudes were used to calculate inter-band correlations with

¹² Modeled signature is provided to us with courtesy of Honzik D., Lockheed-Martin Electronics & Missile Group, 1997.

the filter set given in Figure 2. The correlations in Table 2 show that Bands F1-F6 are more highly correlated, since they all are emitted from the same CO₂ molecule. As the band separation increases, the correlation falls off noticeably. Also, filter F7 exhibits a noticeable negative correlation with bands in CO₂ emission.

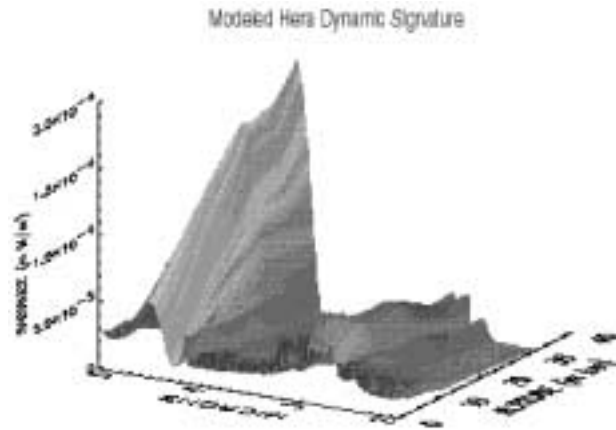


Figure 4. Hera modeled source spectra as a function of altitude

Table 2. Inter-sub-band correlation from modeled Scud data (seven filters defined in notional FPA)

	F6	F5	F4	F3	F2	F1	F7
F6	1.000	0.890	0.932	0.769	0.364	0.239	-0.433
F5		1.000	0.987	0.968	0.734	0.643	-0.092
F4			1.000	0.916	0.626	0.529	-0.241
F3				1.000	0.872	0.799	0.152
F2					1.000	0.990	0.553
F1						1.000	0.616
F7							1.000

3.4 Atmospheric Model Uncertainty

The climate model is characterized by the extinction-coefficient change as a function of altitude. These variation can be analytically estimated using a log-linear regression technique that fits the computed in-band transmittance. The measured parameter for a particular atmospheric type, 76 US Standard Atmosphere as example, is given in Figure 5 for F2, F3, & F4 on the left and for F1 & F6 on the right. The initial extinction coefficient and scale height for these five sub-bands are listed on the figure. The initial extinction coefficients exhibit an order of 40 magnitude variations, 0.046 to 1.67 km⁻¹. The two extremes happened to be on bands, F1 and F6, that are plotted together on the right figure. The atmospheric scale height varies only in an order of 2 magnitude, from 5.8 to 10.4 km. It is of interest to note that the H in first three test bands seem close to 6.73-km, which is the atmospheric scale height above 11 km.

3.5 Predicted Climate Model Variation

One central issue regarding the climate model is the extent of weather variability and its corresponding data uncertainty. This can be defined in many forms. In this work we attempt to define the upper bound of the weather parameter's variability by looking into the parameter's variation across six climate models. Based on MODTRAN established climate, winter and

summer, and the contrast of latitude, namely among sub-arctic, mid-latitude, and tropical, we can observe a first hand variation on the initial extinction coefficient and the scale height. We will use these data to extrapolate how large the weather uncertainty should be in the error budget analysis.

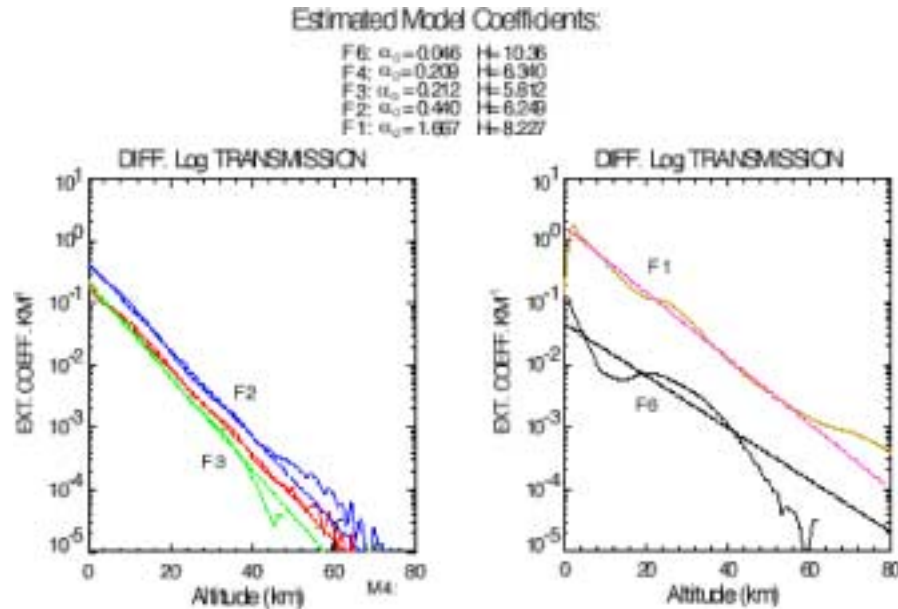


Figure 5. Climate model characterization from MODTRAN computed in-band transmission function. Two log-linear coefficients, as listed on top of the figure, are estimated from each operational band.

Figure 6 illustrates the climate model variation across the six MODTRAN climate types using the same characterization procedure described above. The in-band transmission for F6 and F1 are plotted in the left hand figure and their corresponding extinction coefficient variation, in the right hand figure. From this figure, one can observe that the initial coefficient and scale height for F1 varies very little across these six climate types, $<10\% \sim 30\%$. For F6, the changes are greater, around 200%. Although we do not directly generate seasonal or diurnal variation from MODTRAN runs, we anticipate that the within weather type variation would be smaller. In other words when geographical location and season are fixed, the diurnal induced variation on these two coefficients would be limited to a few percent.

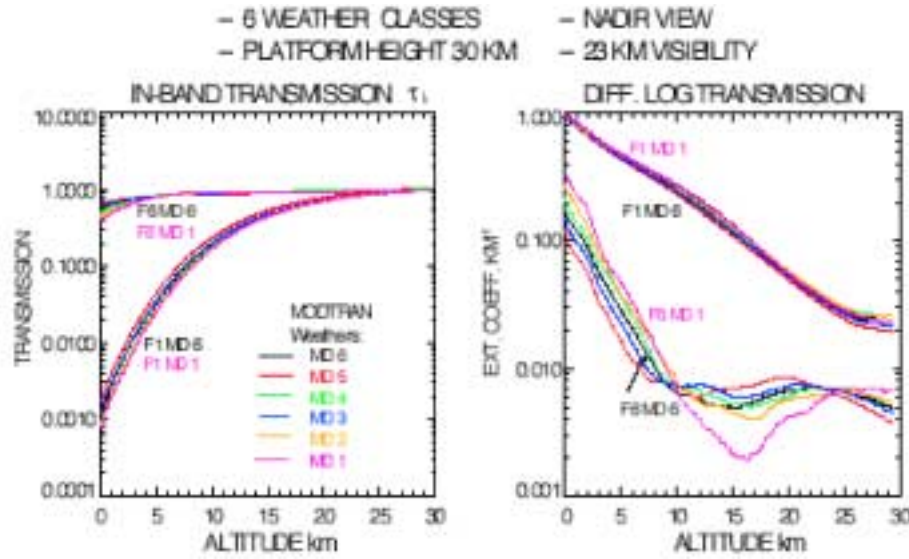


Figure 6. Example of climate model variation based on the initial extinction coefficient and air density scale height

3.6 Geometrical Parameter Uncertainty

The geometry related uncertainty consists of platform position and look angle accuracy. On an HEO orbit, the platform position can be determined quite accurately for the notional FPA based on the known orbit and time. The look angle with the newer pointing control servo, gyro, and star referencing scheme are improved to within a few pixels, namely 20 ~ 30 μ Rad uncertainty or an equivalent of 1.4 to 2.1 km footprint uncertainty at the ground. The anticipated look angle and platform height accuracy are given in Table 3 and included later in Table 4.

Table 3. Geometrical parameter uncertainty for new generation space-borne platform

	Best Accuracy	% Uncertainty	Geolocation Correction	% Uncertainty
Platform Position	10 Meters	0.00003 %	No Improvement	0.00003%
Sensor Look Angle	30 ~ 50 μ Rad	0.03 ~ 0.05 %	3 ~ 5 μ Rad	0.003 ~ 0.005 %

3.7 Measurement Data Uncertainty

The variation in measurement data B is originated from various noise sources embedded in the contrast signature. These include the background subtraction residual (spatial random noise), the short-term temporal fluctuation and the sensor's dark current. Other sensor related noise sources are originated from various signal processings, such as FPA non-uniformity and pixel-gap correction, point source motion compensation, and FPA radiance calibration.

Figure 3 shows the background data statistics derived from the ISTEf HERA data set mentioned earlier. The background (sky) mean radiance is obtained by averaging over the entire pixel per frame whereas the background residual is the 1σ deviation derived from contrast signature where a 5x5 pixel mean removal stencil is used. The inter-frame temporal fluctuation is defined as 1σ deviation of two adjacent frame differences. Due to the plume region changes

dynamically from one frame to the other, the abrupt increases of noise is judged to be originated from the shift of plume location. Thus, the lower bound of the temporal noise is considered as the temporal fluctuation.

As shown in Figure 3 and the last three columns in Table 1, the background spatial noise is $6.0 \mu\text{W}/\text{cm}^2\text{-sr}$, which is 4.7 % relative to the mean background radiation¹³. This fluctuation remains almost constant for the entire 30-second interval. It is also observed that this spatial noise happens to be the same magnitude as that of the temporal fluctuation and is about three times larger than the detector's internal dark current, which is $2.1 \mu\text{W}/\text{cm}^2\text{-sr}$ NER (Noise Equivalent Radiance) estimated from the Raytheon-Amber camera specs, an InSb technology.

Table 4. MPR input data uncertainty estimation from measurements

Parameter	Mean Value	% Uncertainty	Correlation
Plume Source Signature	200.0 ~ 1000.0 $\text{W}/\text{cm}^2\text{-sr}$	3 ~ 6	0.4 ~ 0.8
Extinction Coefficient	0.06 ~ 1.60 km^{-1}	2 ~ 5	0.3 ~ 0.6
Scale Height H	5.0 ~ 11.0 km	2 ~ 10	0.3 ~ 0.5
Look Angle	0 ~ 9.0 ⁰	0.1~ 1.0	
Platform Position	30,000 KM (HEO)	0.01	
Background Residual	2.0 ~ 10.0 $\text{W}/\text{cm}^2\text{-sr}$	3 ~ 5	0.3 ~ 0.6
Foreground Fluctuation	1.0 ~ 2.0 $\text{W}/\text{cm}^2\text{-sr}$	3 ~ 5	0.3 ~ 0.6

3.8 Overall Input Data Statistics

The data uncertainties discussed above are summarized in Table 4. Although some of the supporting data are not shown here, their data uncertainties are provided in the list using our best knowledge. The individual error contributions are not equal, and it is clear, once all the error contributions are evaluated, which of them should be addressed first in order to reduce the net Root-Sum-Squared (RSS) error. Moreover, we now have a rationale for specifying how low we must drive the error in each of the contributing factors if the RSS error goal is to be realized.

4.0 System and Error Budget Assessment

The system configuration for evaluating the total error budget for an MPR system is depicted in Figure 7. The upper box denotes the new addition to MPR that computes the range sensitivity coefficient and parameter uncertainty for the four key error sources. The lower box denotes the existing MPR system with a minor simplification. The operational sequence of this combined system is explained below:

The error budget analysis foundation described in previous section is implemented as a parallel sub-system to the existing AMPR system. Other alternative approach exists. That is the range error can be estimated by Monte Carlo simulation in which noise associated with each source is added to the signal model of the MPR system and repeatedly generate the range estimate and compute their data statistics. However, in current investigation, it is the first approach is used. In a follow-up effort, the second approach should be explored, so that it can

¹³ ISTEf has provided us a calibration constant, a count-to-radiance ($\text{W}/\text{cm}^2\text{-sr}$) conversion constant of 1.3×10^6 , thus, the 7-unit background residue given in Figure 9 yields a $6.0 \mu\text{W}/\text{cm}^2\text{-sr}$ radiance.

provide a more realistic error budget estimation. But one should know that is a time consuming alternative.

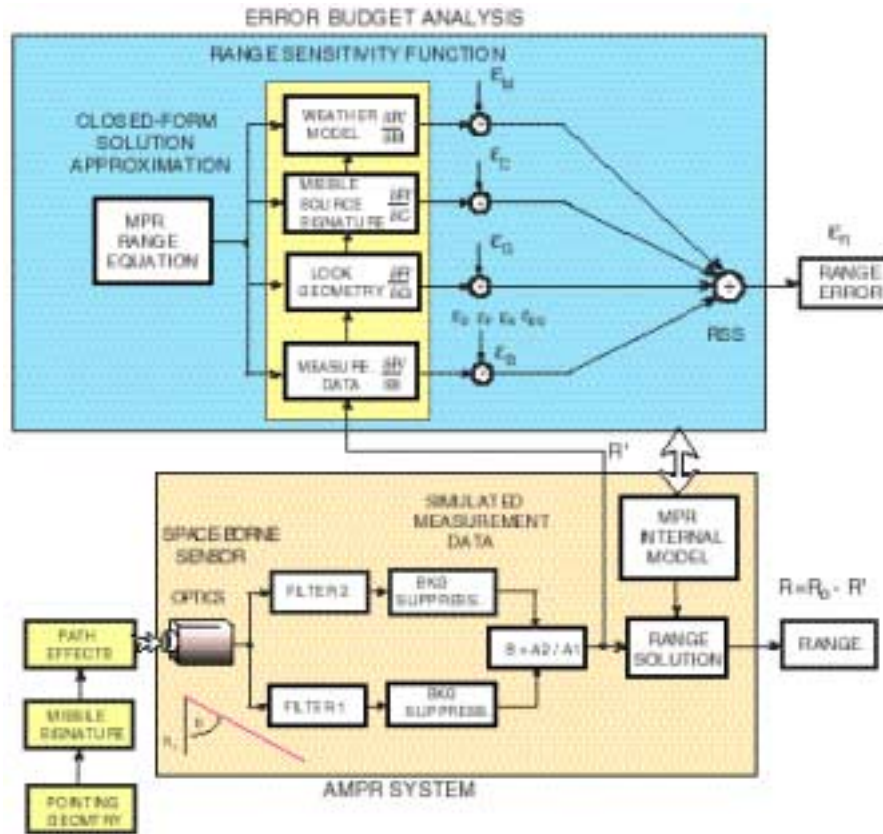


Figure 7. System configuration for error budget analysis

4.1 Example of Total Range Error with 5% Data and Parameter Uncertainties

The total error budget simulation is carried out based on an ICBM surrogate launch observed from an HEO platform. The climate is assumed to be a mid-latitude summer. The platform height is set at 33,000 km with an 8.9° elevation angle. Using the transmissions computed from MODTRAN, the model-based total error budget is generated and plotted in Figure 8. This data is generated based on a common data uncertainty, 5% relative to the mean except the geometry is set at 1%. This result offers a quick estimate on how each error source contributes to the total error budget assuming everything equal. In the figure, the $\pm 1\sigma$ random range errors derived from each of the sources are added up step-by-step to provide an additive growth of overall error figure. This plot can be read as follows:

- (1) estimated range derived from measurement data without noise is plotted as a function of the true range, the solid line in diagonal
- (2) $\pm 1\sigma$ random range error, σ_B derived from measurement with noise (1σ of sensor noise plus 3σ of background residue) are added to the diagonal line. Here the background suppression residual, is represented as three times larger than the NEI

(3) $\pm \sigma_C$, the source signature induced range error is superimposed to (and subtracted from) the previous summed error, the two proceeding curves derived in step two

(4) $\pm \sigma_\phi$, the geometry induced error, viz., zenith angle associated uncertainty is superimposed on curves derived from step 3.

(5) $\sigma_\alpha + \sigma_H$, the climate model induced random range errors, are superimposed on top of the curve derived in step 4. Here, two closely separated curves represent the extinction coefficient and the scale height induced errors, separately. Error induced from H is dominant.

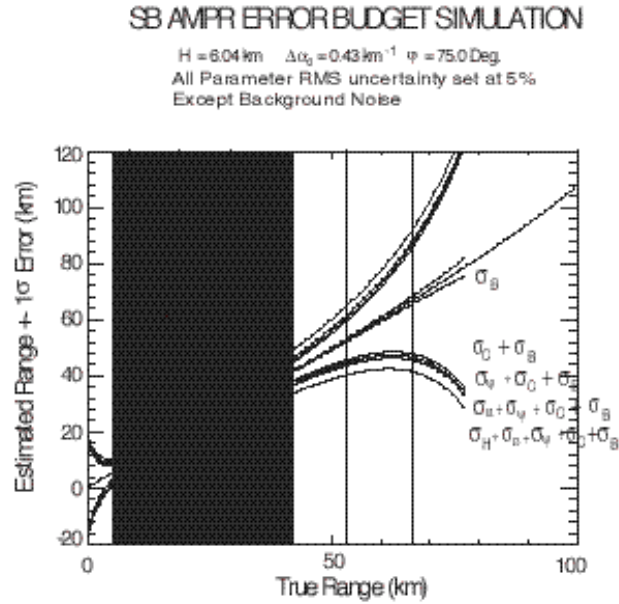


Figure 8. Error budget estimation as a function of R' , the range from target to ground, is plotted for 75° zenith angle. The four curves above and below the true (diagonal black curve) are the errors for: (1) data associated noise σ_B (red curve), (2) source fluctuation σ_C (green), (3) look angle σ_ψ (dark blue), and (4) initial extinction coefficient $\sigma_{d\alpha}$ (brown) and scale height factor σ_H (pink).

For picturing the error contribution from each sources, the data displayed in Figure 8 are re-computed as a percentage value and tabulated in Table 5 as a function altitude. The slant depth at maximum depth for zenith angle of 75° , viz., 280-km is used as the nominal range to derive these percentage value.

Table 5. Total error budget expressed as percentage error with respect to 280-km slant depth

Alt (km)	σ_B Background Residual %	σ_C Source %	σ_ψ Geometry %	σ_α Alpha %	σ_H Scale Height %	% Total Error
0.0	5.183	0.035	0.386	0.347	0.424	6.376
2.5	0.137	0.053	0.228	0.347	0.586	1.350
5.0	0.013	0.078	0.068	0.347	0.749	1.256
7.5	0.003	0.117	0.092	0.347	0.913	1.472
10.0	0.001	0.175	0.253	0.347	1.078	1.855
12.5	0.001	0.263	0.416	0.347	1.244	2.271
15.0	0.001	0.397	0.58	0.347	1.412	2.737
17.5	0.001	0.600	0.746	0.347	1.582	3.276
20.0	0.001	0.913	0.913	0.347	1.754	3.929
22.5	0.001	1.397	1.084	0.347	1.928	4.758
25.0	0.002	2.153	1.256	0.347	2.105	5.864
27.5	0.003	3.346	1.433	0.347	2.285	7.414
30.0	0.004	5.253	1.613	0.347	2.470	9.688

4.2 Rank Order Error Contributions

With all parameters specified at 5% equal uncertainty and have the results shown in two forms of illustration, the error contribution from the five sources can be relatively assessed. The background residual and source signature are shown to be the two most prominent contributors, one dominating at the lower and the other, at the higher altitudes. The scale height and geometry are the two less pronounced factors, but exhibit a similar high-altitude dominant characteristic as that of the source signature. The last and most insignificant error contributor is the atmospheric extinction coefficient, which constitutes only a 0.35% constant error through out the whole altitude.

4.3 Inter-Band Correlation and Error Budget

As mentioned early in Section 2, the range errors in some system parameters must also be accounted for their inter-band correlation. The source signature has been shown to have considerably high correlation. As shown in Table 2, F4, F3, and F2 have exhibited, respectively, a 0.93, 0.77, & 0.46 correlation with F6, the reference band. Using this correlation trend as a basis and assuming a 5% random source uncertainty, the effects of error reduction as a function of correlation, from 0 to 0.99, are graphically illustrated in Figure 9. Obviously, the range error will be reduced as much as 30 to 90%. In other words, if we found that the data uncertainty is 10% but accompanying a 0.60 correlation between bands, the resultant range error could be no greater than we have in column 3 of Table 5 in which it is computed at a 5% uncertainty with no correlation.

In summary: (1) the measurement data accompanied uncertainty dominates the low altitude tracking error; (2) error induced from source uncertainty dominates at higher altitudes; (3) atmospheric scale height error contributes more than the error in atmospheric extinction coefficient; and (4) the error induced from sensor look geometry is more pronounced at high altitudes. The overall nominal RSS error budget for 2.5 km < h < 22.5 km is on the order of 1.4 to 5.0% of the 280-km slant depth and the magnitude increases drastically beyond both ends, near the ground and above 25 km altitudes.

4.4 Filter Toggling Induced Range Error

The MPR algorithm assumes that two bands are measured simultaneously. However, when a pair of bands are toggled, it induces some error due to the changes in target signature, line of sight change, pixel location shift, etc., particularly if there is an appreciable time between the measurements. In order to reduce this error one could use pairs of measured filter samples in one of the two bands to estimate the value of that filter output at points between the samples when the other band is being measured, i.e. interpolate the output of one of the bands. In order to make some estimate of the residual error involved in this interpolation, we consider the simple case where this interpolation is done linearly at the mid point between the pairs of measurements. One can evaluate the mean and the RMS error during the early portion of the flight using a simple signature model. Since it is during this portion of the flight that the rate of change of the missile signature is the largest and the interpolation error is correspondingly large, the analysis will serve to bound the error.

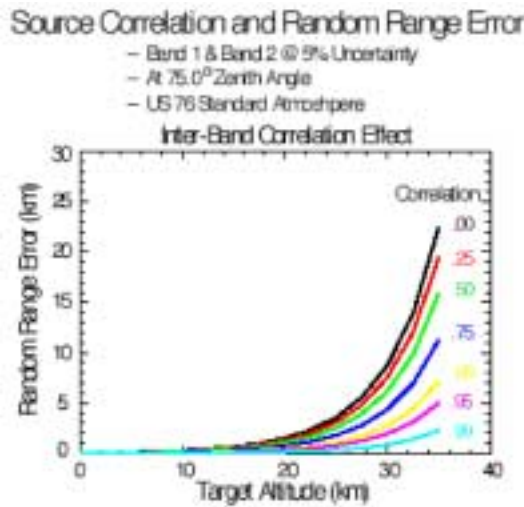


Figure 9. Source related random range error estimated at 5% uncertainty accompanied with various degrees of inter-band correlation, 0.0 to 0.99.

In order to compute these range errors, one must have specific values for various coefficients used in the model. These include $G = \alpha_0 H / \cos \phi$ and $\beta = 1/2 g (T/W - 1)/H$ which in turn depend on the Target acceleration, the atmospheric extinction coefficients α , and scale height H , as well as the target range to the ground, R' , and zenith angle ψ measured at the target. As an example, we will consider a surrogate TBM, the HERA target missile, which during its first stage has an acceleration coefficient $1/2 g (T/W - 1) = 6 \times 10^{-3} \text{ km/s}^2$. Here T and W denote the missile thrust and weight, respectively.

The atmospheric scale height is approximately 6.7 km and the atmospheric extinction coefficients depend upon the spectral bands as shown in Table 2. In the following example, Band 6 will be used as the MPR reference band and the test band is F4. The interpolation will be done on the test band.

The results in Figure 10 show the mean or average interpolation error as a function of interpolation sample time; each of the curves corresponds to a fixed TALO and a fixed viewing angle of 6° at the sensor. It is clear from these results that for this viewing angle and the HERA missile, the mean interpolation error is quite small in most bands when the filter revisit-time is less than 4 seconds. However, the error increases for the more opaque bands where the output signal is smaller. The RMS value of the interpolation error is commensurate with the level of noise in the measurements themselves. Since two samples of the noise are used in the determination of the output there is a factor of $\sqrt{2}$ reduction in the RMS, if the noise samples are un-correlated.

It should be noted however, that these results depend on the missile being observed. A more rapidly accelerating missile than the HERA will have a larger mean interpolation error, and conversely. In addition, the results also depend on the inclination angle of the sensor, with larger maximum error at larger angles.

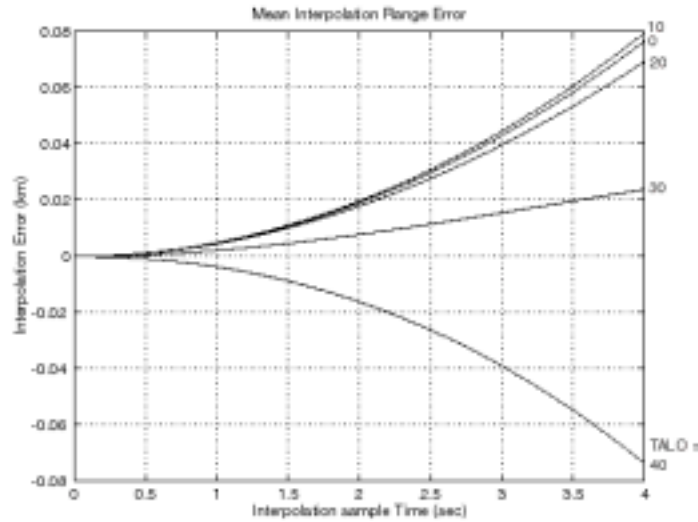


Figure 10. Interpolation mean error using band F2. MPR done with bands F1 and F2

4.5 Overall Error Trends

The analytic error models described below are obtained from the basic analysis of Section 2.2 and implicitly contain information on how these errors vary with key sensor and scenario parameters. We will enumerate some of these in the following:

1) Measurement Associated Range Error

$$\sigma_{R_i} = \exp\left(\frac{h_1}{H}\right) \frac{\sqrt{\left(\frac{N_1}{A_1}\right)^2 + \left(\frac{N_2}{A_2}\right)^2}}{(\alpha_{02} - \alpha_{01})} \quad (15)$$

The range error is clearly inversely proportional to the received target signal-to-noise ratios as well as the difference in the ground level extinction coefficients in each of the two MPR spectral bands. In particular, if the noise source is the same in each band then the range error is directly proportional to its value. An example would be the external or FPA dark current sensor noise characterized by its NEI. The error initially decreases with altitude to a minimum value but then

risks sharply as the exponential factor takes over. This suggests that there is a limited region of MPR utility for this band pair and that other band combinations must be used to cover higher altitude regions. This requirement for band switching has been pointed out in an earlier work¹⁴.

2) Data Processing Range Error

$$\sigma_{R_i} = \exp\left(\frac{h_i}{H}\right) \left[\sqrt{2} \frac{\sigma_{DP}}{A} \right] \frac{1}{(\alpha_{02} - \alpha_{01})} \quad (16)$$

The general nature of this error source is essentially the same as the measurement error. However, it should be noted that the data processing error sources could either be essentially independent of the apparent source signature, i.e. an additive error such as residual background subtraction error, or proportional to the source signature, i.e. multiplicative error, such as variations in in-band gains across bands. In the former case the net target signal to noise would tend to increase with altitude producing the initial drop in error discussed above. On the other hand, the latter error source generates a proportional error, which would not cause such an increase, and the shape of the error vs. altitude curve is an exponentially increasing function.

3) Source Signature Uncertainty Range Error

$$\sigma_{R_i} = \exp\left(\frac{h_i}{H}\right) \frac{\ln \frac{C_a}{C_0}}{(\alpha_{02} - \alpha_{01})} \quad (17)$$

This error source could be due to uncertainty in the assumed source spectral intensity used in the MPR algorithm, or random changes in the plume signature due to its dynamic nature. In both cases the error is generally proportional to the nominal values, although the proportionality factor may change with altitude or equivalently, time into the motor burn. The net effect is an exponentially increasing range error component.

4) Atmospheric Absorption Uncertainty Range Error

$$\sigma_{R_i} = \frac{H}{\cos \phi} \left[\frac{\sigma_{(\alpha_{02} - \alpha_{01})}}{(\alpha_{02} - \alpha_{01})} + \left[1 + \frac{h_i}{H} \right] \frac{\Delta H}{H} \right] \quad (18)$$

The atmospheric uncertainty error has two components both of which have proportionate error terms, but the second also has a target altitude multiplier. The net effect is an error that has a linearly increasing term superimposed on a constant value. The origin of the two error sources is intimately related and is the result of atmospheric changes due to diurnal as well as seasonal effects. It is assumed that the long term seasonal as well as the basic night and day cyclic changes can be compensated by typical weather observational measurements. The random changes due to small scale turbulence effects, however, form a baseline error source that can not be compensated. In addition one may want to allow for weather front changes whose precise timing can not be foreseen, unless of course one has independent instrumentation to constantly monitor the atmosphere and provide appropriate corrections to the MPR algorithm.

5) Line of Sight Uncertainty Range Error

¹⁴ cf Chuang et al., 1997 IRIS Meeting Proceedings.

$$\sigma_{R_i} = (h_i + H) \frac{\sin \phi}{\cos^2 \phi} \sigma_\phi \quad (19)$$

This error component has both a constant and a linearly increasing term with altitude. The basic source of the error is the uncertainty of the elevation of the line of sight to the target in the atmosphere.

5.0 Application Example

The error budget established so far gives a reasonable estimation of the overall random range uncertainty for an MPR system. Within the 2 km to 15 km altitude operation using the first band pair, the error is 1.5% to 2.7%, viz., 4.5 to 7.0 km at 280 km slant depth. With the space-borne sensor pointing accuracy rated at 30 to 50 μ Rad as estimated in Table 3, the azimuth-elevation uncertainty would be 0.9 km to 1.5 km for a nominal 30,000-km range of a HEO platform. Although the combined 3-D error probability is an oval shape, we will treat it as a 4.5 km Spherical Error Probability (SEP) for simplicity. Based on the investigation carried out earlier¹⁵, significant improvement can be achieved by applying missile-trajectory estimation technique to the MPR generated position vectors. When optimal estimation techniques were applied to portions of the 60-second TBM boost phase position sequence, the resultant Elliptical Error Probability (EEP) for a single-stage TBM is shown to improve by factors of four to ten depending on the data length, a function of cloud-cover height. Using this result to extrapolate the 4.5-km position SEP, a 1-km SEP of the Predicted Acquisition Point (PAP), at 64% confidence level could be achieved.

Using this TBM reporting capability of a space-borne sensor system to cue a ground or airborne missile defense system and to guide its interceptor, there are at least three or four alternative intercepting schemes^{16,17,18}. These are intercepting the TBM during its boost phase (BPI), missile ascending phase (API), mid course (MCI), or at terminal flight (TFI). Some of these schemes, in fact, have already been explored: ABL or UAV/KKV for BPI, THAAD for MCI, and Patriot PAC III for TFI. In all of the cases, the requirement for cueing the subsequent weapon system's surveillance sensor is the PAP specified by the space-borne sensor that must be given at high confidence of probability, e.g., 99%. At this level, the SEP is defined approximately as 3σ . Using the example given above, it would be a 4.5 km. See Figure 11 for a graphic rendering of this sensor-interceptor cueing scenario. If the sensor platform to be cued is a UAV loitering within 100-km of the TBM launch site inside hostile enemy territory, the 0.03x0.03 str view in space can be completely covered by an IR sensor with 256x256 FPA technology. Thus, the MPR is capable of achieving a hand-over basket that is needed by a missile for terminal guidance^{19,20}.

¹⁵ Cf. Perlman et al., IRIS Passive Sensor, 1997.

¹⁶ Eshel David, "Sending in the Scudbusters," Unmanned Vehicles October, 1997.

¹⁷ Zarchan P., "Midcourse Guidance Strategies for Exoatmospheric Intercept," N00174-97-D-0030/0005, NSWCD at Dahlgren, VA, 1997.

¹⁸ R. Hintz, G. Goetz, NAWC-WD, W. Hietzke, SAIC, "Candidate Boost Phase Intercept (BPI) Sensor Suite for Unmanned Air Vehicle (UAV)," 1998 IRIS Passive Sensors Vol. II.

¹⁹ Nesline P.W., Zarchan P., "A New Look at Classical vs Modern Homing Missile Guidance," Jour. Of Guidance and Control, Vol. 4 No. 1, January, 1981.

²⁰ Cf. Draper et al., AIAA/BMDO TR Symposium 1998.

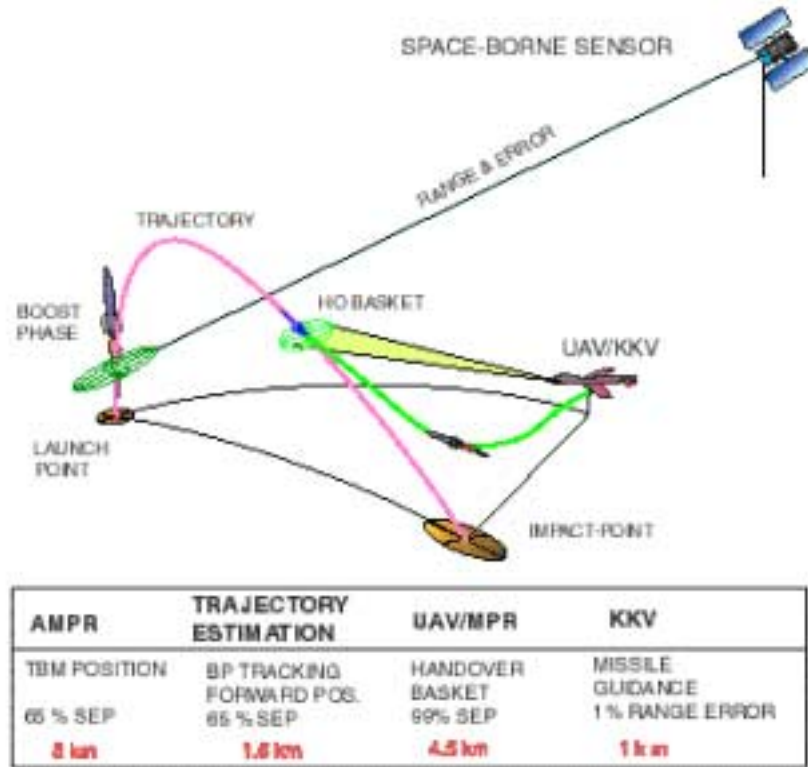


Figure 11. Space-borne MPR sensor to airborne UAV/KKV cueing application example

6.0 Conclusions

In an MPR system the individual error contributions are not equal and are dependent on the environment. We have shown that the measurement data and source signature uncertainty are the two most pronounced components of the MPR range error. When reduction measures are applied, we anticipate that the overall random range error can be reduced below 2% of the maximum slant depth.

The most influential error component in the MPR system is the uncertainty associated with the measurement data. This component consists of both external noise sources (e.g., image processing residual, calibration related non-uniformity etc.) and the internal noise sources (e.g., the detector, sensor optic and electronic noise). Range errors could be reduced by improving the design of sensor optics, selection of detector material, and the optimization of signal processing algorithms. The background clutter residual can also be reduced by variety of suppression techniques.

The range error induced by the source signature is next. This error arises from the uncertainty in internal representation of the slow changing plume radiation and their short-term fluctuations. By implementing a dynamic spectral template varying as a function of missile altitude and accounting for inter-band correlation, the RSS error induced by this factor can be limited to <2%.

The third error contribution is the atmospheric modeling uncertainty. The differential extinction coefficient plays a key role in reducing RSS error. However, the inaccuracy in representing the scale height, a non-differential term, is critical. An effort in validating this atmospheric scale height for local weather representation is thus recommended.

The last error source is the pointing geometry related uncertainty. The target look angle is expected to register better than 0.1-% accuracy, so that the geometry-induced error would be smallest source of all.